Journal of Computational Physics 230 (2011) 329–348

Contents lists available at ScienceDirect

Journal of Computational Physics

journal homepage: www.elsevier.com/locate/jcp

Modeling and simulation of fish-like swimming

M. Bergmann *, A. Iollo

INRIA Bordeaux – Sud Ouest, Equipe-projet MC2, 33405 Talence, France
Institut de Mathématiques de Bordeaux, UMR 5251, Université Bordeaux 1, 33405 Talence, France

ARTICLE INFO

Article history:
Received 24 February 2010
Received in revised form 9 September 2010
Accepted 10 September 2010
Available online 29 September 2010

Keywords:
Fluid–structure interaction
Penalization method
Fish swimming

ABSTRACT

Modeling and simulation of two-dimensional flows past deformable bodies are considered. The incompressible Navier–Stokes equations are discretized in space onto a fixed cartesian mesh and the displacement of deformable objects through the fluid is taken into account using a penalization method. The interface between the solid and the fluid is tracked using a level-set description so that it is possible to simulate several bodies freely evolving in the fluid. As an illustration of the methods, fish-like locomotion is analyzed in terms of propulsion efficiency. Underwater maneuvering and school swimming are also explored.

1. Introduction

The simulation of complex flows such as fluid–structure interactions, freely moving objects or flapping wings necessitates the development of ad hoc methods that bypass the complications induced by moving grids. These methods, such as the immersed-boundary method (see for a review [1]) or the augmented Lagrangian approach [2,3] represent a compromise between accuracy and actual feasibility of a simulation. Here we revisit the penalization method [4] and show how to couple it with level sets to simulate a paradigmatic case of interaction between freely evolving objects and an incompressible flow: fish-like swimming.

The modeling and simulation of fish-like swimming is of interest in life sciences as well as in engineering applications. Understanding the mechanics of swimming can help in clarifying some aspects of the biological evolution and of the physiology of aquatic organisms. In engineering the study and optimization of aquatic locomotion can improve the design of underwater vehicles having superior maneuvering capabilities. More generally, many other technological applications ranging from the sedimentation of granular flows to the simulation of a maneuvering aircraft can benefit from the efficient modeling of the unsteady interaction between the flow and moving objects.

Among the first mathematical results concerning fish-like swimming were those reported by Lighthill in a series of papers [5–8]. The main results were derived in the context of a linearized approach for an inviscid flow. Since then, many other papers were dedicated to the study of inviscid flows and a complete survey of this literature is given in [9]. A more recent example is presented in [10], where a numerical method for the dynamics of a flexible body in an inviscid flow is described.

For fish-like swimming in viscous flows less results are known and they are mainly experimental. In particular in [11] an experimental set-up is designed to investigate the drag reduction mechanism in fish-like locomotion using a thunniform robot. The most striking result is that the power that the robot needs to swim at a given speed is less than that required to tow it at the same speed. Even more striking is the possibility of passively extracting energy from a vortex wake: in [12] it is shown that a dead fish is propelled upstream by the coupling between the oncoming vortices and the flexible body.

* Corresponding author at: INRIA Bordeaux-Sud Ouest, Equipe-projet MC2, 33405 Talence, France.
E-mail address: Michel.Bergmann@inria.fr (M. Bergmann).

0021-9991/$ - see front matter © 2010 Elsevier Inc. All rights reserved.
doi:10.1016/j.jcp.2010.09.017

Motivated by these examples, in this paper we study fish-like swimming in the two-dimensional low-Reynolds number case. Even though the experimental results cited are relevant to three-dimensional flows at a Reynolds number such that the flow is in the turbulent regime, the two-dimensional laminar case is of interest since numerical results for viscous flows are scarce. This is mainly due to the fact that simulations performed with standard methods are costly in terms of computational time and difficult to set up. Nevertheless, even at low Reynolds numbers three-dimensional wakes show some distinctive features that can in principle affect the swimming mechanism.

Classical approaches to simulate moving bodies through fluids require body fitted meshes that must be deformed and periodically rebuilt to cope with the body displacements. More recently, methods based on fixed cartesian meshes that avoid these shortcomings were developed [13,4]. These methods are based on the idea of modeling the presence of a solid body by appropriate volume forces. Other investigations in this sense have been recently carried out. In [3] the interaction between a rigid body and an incompressible viscous flow is modeled by considering the actual fluid flow and the rigid body motion as a single flow subject to a volume force acting in the domain occupied by the rigid body. This force is proportional to the local deformation tensor so that a rigid displacement is imposed in the limit. Mathematically this approach can be interpreted as a minimization of the residuals in an appropriate finite-element space with a penalization on the norm of the deformation tensor in the region occupied by the rigid body. Moving bodies through a fluid flow are investigates also in [14]. A single fluid approach is still used but in this work the penalization term acts on the velocity field in the region of the rigid body, thus relaxing some numerical difficulties arising when penalizing the norm of the velocity gradient. Yet another approach, developed in [2] is based on a fictitious domain formulation: the rigid bodies are filled by the surrounding fluid, and the constraint of rigid body motion is relaxed by introducing a distributed Lagrange multiplier. This method has been extended to self-propelling bodies in [15,16], where the authors show examples of fully resolved three-dimensional simulations of fish-like swimming.

The scope of the paper is therefore twofold. We present a simulation technique that is an extension to moving objects of [4] and we apply it to the study of different swimming modes. In particular we are concerned with the power required for swimming as a function of the swimming modes and eventually of the relative position of the swimmers.

2. Flow configuration and governing equations

Our objective is to study the two dimensional incompressible flow around N_s moving and deformable bodies. The entire domain is noted $\Omega = \Omega_f \cup \Omega_i$, where the domain Ω_f is filled with fluid of constant density ρ and dynamic viscosity μ. The domains Ω_i represent deformable moving bodies of densities ρ_i. Let us denote the velocity of $x_i \in \Omega_i$ by $\boldsymbol{u}_i$. Fig. 1 presents a sketch of the flow configuration under consideration.

The flow is governed by the incompressible Navier–Stokes equations

$$\rho\left(\frac{\partial \boldsymbol{u}}{\partial t} + (\boldsymbol{u}\cdot\nabla)\boldsymbol{u}\right) = -\nabla p + \mu\Delta\boldsymbol{u} \quad \text{in } \Omega_f, \tag{1a}$$

$$\nabla\cdot\boldsymbol{u} = 0 \quad \text{in } \Omega_f, \tag{1b}$$

$$\boldsymbol{u} = \boldsymbol{u}_i \quad \text{on } \partial\Omega_i, \quad i = 1, N_s \tag{1c}$$

with initial condition in Ω and boundaries conditions on $\partial\Omega$. The velocity $\boldsymbol{u}_i$ in Eq. (1c) will result from the interaction between the fluid and the body deformation as explained in the next sections.

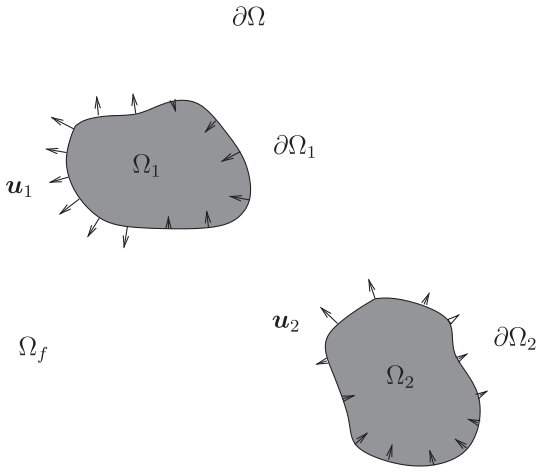

Fig. 1. Sketch of the flow configuration.

2.1. Penalization model and level set functions

The whole system is described as a single fluid flow of density ρ where the bodies past which the flow is computed are modeled using the so-called penalization method [4]. This approach consists in considering the regions corresponding to Ω_i as a porous media with a very small permeability $K \ll 1$.

Let χ_i denote the characteristic function for the ith body, so that

$$\chi_i(\boldsymbol{x}, t) = 1 \quad \text{if } \boldsymbol{x} \in \Omega_i, \tag{2}$$

$$\chi_i(\boldsymbol{x}, t) = 0 \quad \text{elsewhere}. \tag{3}$$

In the limit of $K \to 0$ it can be shown, see [4], that system (1) can be written on the whole domain Ω as follows:

$$\rho\left(\frac{\partial \boldsymbol{u}}{\partial t} + (\boldsymbol{u}\cdot\nabla)\boldsymbol{u}\right) = -\nabla p + \mu\Delta\boldsymbol{u} + \frac{\rho}{K}\sum_{1=1}^{N_s}\chi_i(\boldsymbol{u}_i - \boldsymbol{u}) \quad \text{in } \Omega, \tag{4a}$$

$$\nabla\cdot\boldsymbol{u} = 0 \quad \text{in } \Omega, \tag{4b}$$

with initial conditions in Ω and boundaries conditions onto $\partial\Omega$. The velocities at the boundaries of the immersed objects are imposed through the penalization terms $\frac{1}{K}\sum_{1=1}^{N_s}\chi_i(\boldsymbol{u}_i - \boldsymbol{u})$. Eqs. (4a) and (4b) can be discretized onto cartesian grids, avoiding the use of body fitted meshes.

The flow depends explicitly on both the body positions and velocities via the penalization term. However, in the study of self propulsion these velocities are not imposed and depend in turn on the flow field. Additional equations for $\boldsymbol{u}_i$ and χ_i must be provided to close system (4a) and (4b). The first relationship can be formally written as:

$$\dot{\boldsymbol{u}}_i = \mathcal{F}(\boldsymbol{u}, p, \boldsymbol{P}_1, \ldots, \boldsymbol{P}_{N_s}), \quad i = 1, \ldots, N_s; \tag{4c}$$

where $\mathcal{F}$ (Newton's laws of motion) denotes a function to be specified in Section 4, and $\boldsymbol{P}$ is a control vector that defines the shape and deformation speed of the ith body. The detailed description of the deformation is the purpose of Section 5.

The final equation to close the system describes the displacement of χ_i by the advection velocity $\boldsymbol{u}$:

$$\frac{\partial \chi_{s_i}}{\partial t} + (\boldsymbol{u}\cdot\nabla)\chi_{s_i} = 0, \quad i = 1, \ldots, N_s, \tag{4d}$$

where $\boldsymbol{u} = \boldsymbol{u}_i$ for $x \in \partial\Omega_i$. For later convenience we introduce a level set function ϕ_i that represents the signed distance function of a given point to $\partial\Omega_i$ [17]. It is negative if $x \in \Omega_i$ and positive elsewhere. The level set $\phi_i = 0$ is the interface between the fluid and the bodies immersed in the flow. The characteristic function can be deduced from ith distance function as $\chi_i = 1 - H(\phi_i)$ where H is the Heaviside function. The level set functions satisfy the same advection equation as the characteristic functions

$$\frac{\partial \phi_i}{\partial t} + (\boldsymbol{u}\cdot\nabla)\phi_i = 0, \quad i = 1, \ldots, N_s. \tag{5}$$

3. Numerical solution

The equation are discretized in non-dimensional form. The dimensionless system is obtained using as a reference length L the chord of the immersed body, the reference velocity U_0, time L/U_0, density ρ and pressure $p_0 = \rho U_0^2 L$. The Reynolds number is defined in accordance.

3.1. Solution of the fluid–body interaction

The main idea is to decouple the flow solution from the motion of the immersed bodies. At iteration n the velocity and pressure fields $\boldsymbol{u}^n$, p^n are given as well as the positions and velocities of the immersed bodies χ_i^n and $\boldsymbol{u}_i^n$, respectively. The flow solution at the next time step $\boldsymbol{u}^{n+1}$ and p^{n+1} is found by assuming that χ_i^n and $\boldsymbol{u}_i^n$ stay constant over Δt. Let $\mathcal{NS}(\boldsymbol{u}, p)$ be the Chorin–Temam discrete Navier–Stokes operator defined in the next section.

The time integration scheme for the fluid–body interaction is the following:

(1) compute the flow field $\boldsymbol{u}^{n+1}$ given $\boldsymbol{u}^n$ and the positions and velocities of the immersed bodies at iteration n

$$\frac{\boldsymbol{u}^{n+1} - \boldsymbol{u}^n}{\Delta t} = \mathcal{NS}(\boldsymbol{u}^n, p^n) + \frac{1}{K}\sum_{1=1}^{N_s}\chi_i^n(\boldsymbol{u}_i^n - \boldsymbol{u}^{n+1}) \quad \text{in } \Omega, \tag{6a}$$

$$\nabla\cdot\boldsymbol{u}^{n+1} = 0 \quad \text{in } \Omega, \tag{6b}$$

(2) compute the positions and velocities of the deformable objects at iteration $n+1$:

$$\boldsymbol{u}_i^{n+1} = \boldsymbol{u}_i^n + \Delta t\mathcal{F}(\boldsymbol{u}^{n+1}, p^{n+1}, \boldsymbol{c}_i^{n+1}), \tag{6c}$$

$$\chi_i^{n+1} = \chi_i^n - \Delta t(\boldsymbol{u}_i^{n+1}\cdot\nabla)\chi_i^n. \tag{6d}$$

This scheme is consistent and first order time accurate. Function $\mathcal{F}$ is detailed in (Section 4).

The penalization error $\|\boldsymbol{u} - \boldsymbol{u}_i\|$, i.e., the error in the Dirichlet boundary condition on the ith body, is inversely proportional to the penalization parameter K. An explicit penalization scheme is stable if $K \leqslant 1/\Delta t$, where Δt is the time step used to discretize the Navier–Stokes equations, so that $\|\boldsymbol{u} - \boldsymbol{u}_{s_i}\| = O(\Delta t)$. Therefore, in order to increase K and to keep reasonable time steps, an implicit scheme must be employed [14]. In what follows an implicit penalization is thus used with $K = 10^{-8}$.

3.2. Time integration

We now focus on the time discretization of system (6a) and (6b). We use a predictor–corrector fractional step method based on the Chorin–Temam schemes [18,19]. The prediction step consists in solving a first fractional step to get $\boldsymbol{u}^*$, where an initial guess for the pressure field, p^*, is given:

$$\frac{\boldsymbol{u}^* - \boldsymbol{u}^n}{\Delta t} = -(\boldsymbol{u}^n \cdot \nabla)\boldsymbol{u}^n - \nabla p^* + \frac{1}{Re}\Delta \boldsymbol{u}^n + \frac{1}{K}\sum_{1=1}^{N_s} \chi_i^n(\boldsymbol{u}_i^n - \boldsymbol{u}^*) \quad \text{in } \Omega. \tag{7}$$

In general this velocity field does not satisfy the continuity Eq. (6b). Hence, the correction step consists in solving a second fractional step:

$$\frac{\boldsymbol{u}^{n+1} - \boldsymbol{u}^*}{\Delta t} = -(\nabla p^{n+1} - \nabla p^*) \quad \text{in } \Omega. \tag{8}$$

Since we want $\nabla \cdot \boldsymbol{u}^{n+1} = 0$, taking the divergence of Eq. (8) we have

$$\Delta\big(\Delta t(p^{n+1} - p^*)\big) = \nabla \cdot \boldsymbol{u}^* \quad \text{in } \Omega. \tag{9}$$

The Laplace operator on the left-hand side is discretized on the uniform cartesian mesh. The discrete divergence operator on the right-hand side regularizes the Dirac mass on the fluid–body interfaces resulting from the gradient of χ_i^n.

Let us denote $\phi = \Delta t(p^{n+1} - p^*) = \Delta^{-1}(\nabla \cdot \boldsymbol{u}^*)$ the solution of the Poisson Eq. (9), the correction step leads to:

$$p^{n+1} = p^* + \frac{\phi}{\Delta t}, \tag{10a}$$

$$\boldsymbol{u}^{n+1} = \boldsymbol{u}^* - \nabla\phi. \tag{10b}$$

The Poisson equation is solved with homogeneous Neumann boundary conditions on $\partial\Omega$ by a fast Poisson solver thanks to the uniform grid. The Neumann boundary conditions ensure that in the correction step the normal velocity at the boundary is not perturbed.

We finally obtain

$$\frac{\boldsymbol{u}^{n+1} - \boldsymbol{u}^n}{\Delta t} = \mathcal{NS}(\boldsymbol{u}^n, p^n) + \frac{1}{K}\sum_{1=1}^{N_s} \chi_i^n(\boldsymbol{u}_i^n - \boldsymbol{u}^{n+1}) \quad \text{in } \Omega, \tag{11}$$

where

$$\mathcal{NS}(\boldsymbol{u}^n, p^n) = -(\boldsymbol{u}^n \cdot \nabla)\boldsymbol{u}^n - \nabla p^* + \frac{1}{Re}\Delta \boldsymbol{u}^{n+1} - \big(\nabla p^{n+1} - \nabla p^*\big). \tag{12}$$

As for space discretization, since we used a penalty model, it is performed on a cartesian grid. We use a centered second order finite-difference approximation for the diffusive term and an upwind third-order scheme for the convective terms. This scheme results in very simple coding for which a parallel implementation is feasible with a reduced development effort. Also grid partitioning is a trivial issue in this context.

4. Laws of motion of the deforming bodies

4.1. Translation and rotation velocities

The velocity of each immersed body can be decomposed into a translation velocity $\overline{\boldsymbol{u}}_i$ relative to the center of mass, a rotation velocity $\boldsymbol{u}_i^\theta$ about this point and a deformation velocity $\boldsymbol{u}_i'$. In the following the deformation velocity is imposed, whereas the translation and rotation velocities are computed using Newton's laws.

Noting $\boldsymbol{F}_i$ and $\boldsymbol{\mathcal{M}}_i$ the forces and the torques exerted by the fluid onto the ith body, the translation velocity $\overline{\boldsymbol{u}}_i$ and the angular velocity $\boldsymbol{\Omega}_i$ are obtained by integrating the following equations

$$m_i \frac{\mathrm{d}\overline{\boldsymbol{u}}_i}{\mathrm{d}t} = \boldsymbol{F}_i, \tag{13a}$$

$$\frac{\mathrm{d}J_i\boldsymbol{\Omega}_i}{\mathrm{d}t} = \boldsymbol{\mathcal{M}}_i, \tag{13b}$$

with m_i the mass of the ith body and J_i its inertia matrix. Given the angular velocity, the rotation velocity is given by $\boldsymbol{u}_i^{\theta} = \boldsymbol{\Omega}_i \wedge \boldsymbol{r}_i$ where $\boldsymbol{r}_i = \boldsymbol{x} - \boldsymbol{x}_i^G$ and $\boldsymbol{x}_i^G$ is the center of mass.

Introducing the dimensionless stress tensor $\mathbb{T}(\boldsymbol{u}, p) = -p\boldsymbol{I} + \frac{1}{Re}(\nabla \boldsymbol{u} + \nabla \boldsymbol{u}^T)$ and $\boldsymbol{n}_i$ the unit outward vector to $\partial\Omega_i$, the forces and the torques exerted by the fluid onto the bodies are:

$$\boldsymbol{F}_i = -\int_{\partial\Omega_i} \mathbb{T}(\boldsymbol{u}, p)\boldsymbol{n}_i \mathrm{d}\boldsymbol{x}, \tag{14a}$$

$$\mathcal{M}_i = -\int_{\partial\Omega_i} \boldsymbol{r}_i \wedge \mathbb{T}(\boldsymbol{u}, p)\boldsymbol{n}_i \mathrm{d}\boldsymbol{x}. \tag{14b}$$

Since the mesh nodes do not fit the body geometries, and because of the order one accuracy, the computation of (13a) and (13b) cannot be performed in this form.

Instead, we consider a time dependent arbitrary domain Ω_{f_i} only surrounding Ω_i (see Fig. 2) such that the force expression becomes:

$$\boldsymbol{F}_i = -\frac{\mathrm{d}}{\mathrm{d}t}\int_{\Omega_{f_i}(t)} \boldsymbol{u}\mathrm{d}V + \int_{\partial\Omega_{f_i}(t)} (\mathbb{T} + (\boldsymbol{u} - \boldsymbol{u}_i) \otimes \boldsymbol{u})\boldsymbol{n}_i \mathrm{d}S - \int_{\partial\Omega_i(t)} ((\boldsymbol{u} - \boldsymbol{u}_i) \otimes \boldsymbol{u})\boldsymbol{n}_i \mathrm{d}S. \tag{15a}$$

A similar equation can be derived for the torque:

$$\boldsymbol{\mathcal{M}}_i = -\frac{\mathrm{d}}{\mathrm{d}t}\int_{\Omega_{f_i}(t)} \boldsymbol{r}_i \wedge \boldsymbol{u}\mathrm{d}V + \int_{\partial\Omega_{f_i}(t)} \boldsymbol{r}_i \wedge (\mathbb{T} + (\boldsymbol{u} - \boldsymbol{u}_i) \otimes \boldsymbol{u})\boldsymbol{n}_i \mathrm{d}S - \int_{\partial\Omega_i(t)} \boldsymbol{r}_i \wedge ((\boldsymbol{u} - \boldsymbol{u}_i) \otimes \boldsymbol{u})\boldsymbol{n}_i \mathrm{d}S. \tag{15b}$$

Note that the integrals on $\partial\Omega_i$ in Eqs. (15a) and (15b) vanish in many applications ($\boldsymbol{u} = \boldsymbol{u}_i$), except for the particular case of transpiration boundary conditions, as in the case of blowing and suction at the border. In the following computations the control volumes Ω_{f_i} are small rectangles surrounding the bodies and fitting the mesh nodes.

4.2. Numerical validation

4.2.1. Space and time accuracy

We compute the L^2 norm, E, of the difference between the numerical velocity field $\boldsymbol{u}$ and the exact one $\boldsymbol{u}^e$ for the Green–Taylor vortex at $Re = 100$. The computational domain is $\mathcal{D} = \{(x, y, t) \in [0, \pi] \times [0, \pi] \times [0, T]\}$ and the error is computed at the final time $T = 1$. The interior scheme space and time accuracy are computed imposing $\boldsymbol{u}^e(x, t)$ on the exterior boundary $\partial\Omega$. As expected, the numerical scheme is first order in time and second order in space (see Fig. 3). We now focus on the penalization order. The Green–Taylor test case is not trivial since the penalized velocity will depend on both time and space. A cylinder centered in $(\pi/2, \pi/2)$ with diameter $D = 1$ is considered. It is immersed in the fluid region where we impose the exact velocity on $\partial\Omega$. If $\boldsymbol{u}_i(\boldsymbol{x}, t) = \boldsymbol{u}^e(\boldsymbol{x}, t)$ inside the circle, then second order in space is recovered. The penalized velocity $\boldsymbol{u}_i(\boldsymbol{x}, t) = \boldsymbol{u}^e(\boldsymbol{x}_{\phi=0}, t)$ is now imposed, where $\boldsymbol{x}_{\phi=0}$ denotes the closest point to $\boldsymbol{x}$ onto the cylinder boundary. The penalization scheme then leads to first order space resolution (see Fig. 3(a)). It is possible in principle to improve the penalization order using both velocity gradients and level set information as done in [20].

4.2.2. Force and torque computation

A two-dimensional flow around a circular cylinder is considered, see Fig. 4. We are interested in computing and validating the aerodynamic coefficient $\boldsymbol{C} = \boldsymbol{F}/(\rho u_r^2 D/2)$, where $u_r = |\boldsymbol{u}_s - \boldsymbol{u}_\infty|$ is a reference velocity and $\boldsymbol{u}_\infty$ the velocity at the infinity of the body. For the following test case, the mesh is of $N_X = 900$ and $N_Y = 600$ nodes uniformly distributed between $x = -6$ and

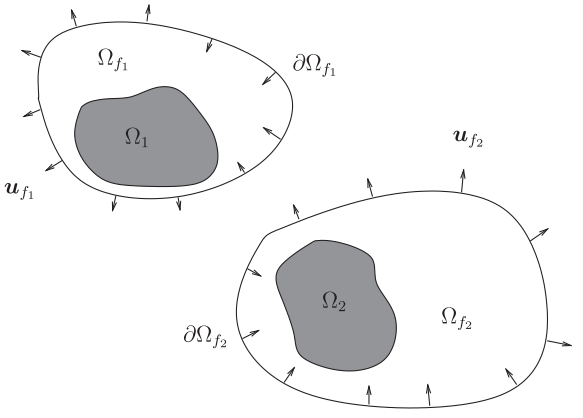

Fig. 2. Sketch of domain used to computed the forces. All geometries and velocity fields are given arbitrarily.

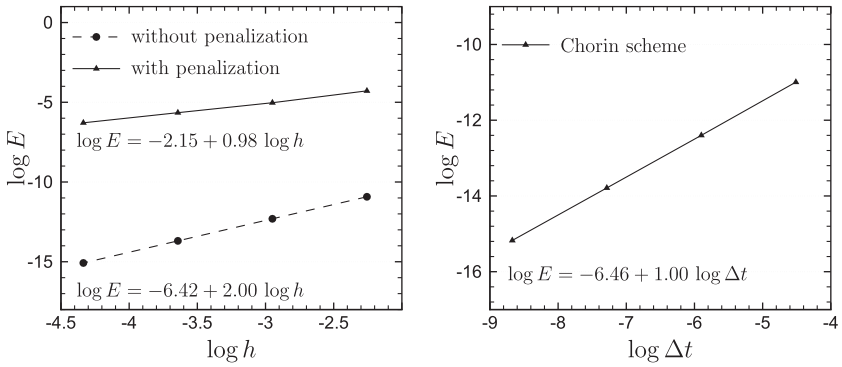

(a) Space accuracy. (b) Time accuracy.

Fig. 3. Numerical scheme accuracy order. Left: the CFL is fixed. Right: $\Delta t = 10^{-2} Re \Delta x^2$

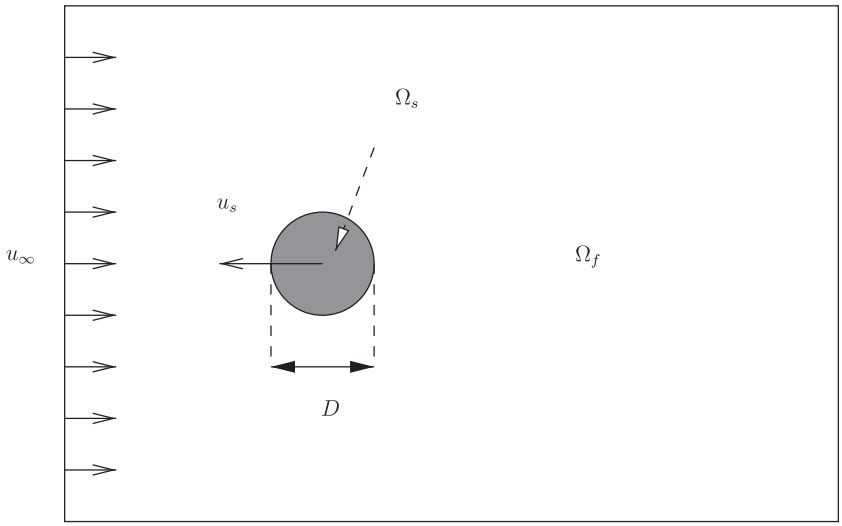

Fig. 4. Sketch of the flow around a circular cylinder.

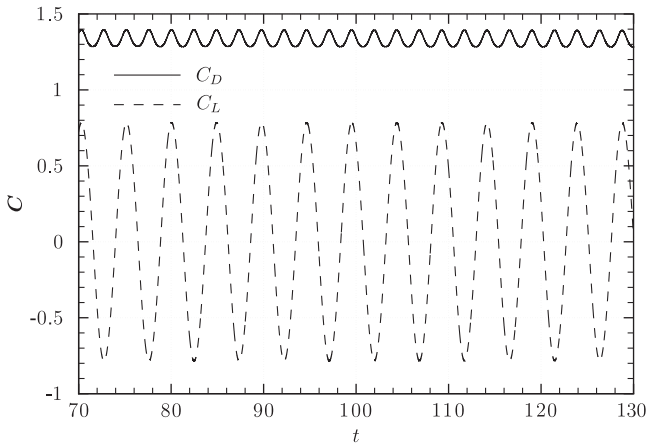

Fig. 5. Temporal evolution of the lift (dashed line) and the drag (solid line) at $Re = 200$.

$x = 12$ and between $y = -6$ and $y = 6$, respectively. The time step is $\Delta t = 0.002$. We define the drag and lift coefficients as $C_D = \mathbf{C} \cdot \boldsymbol{e}_x$ and $C_L = \mathbf{C} \cdot \boldsymbol{e}_y$, respectively.

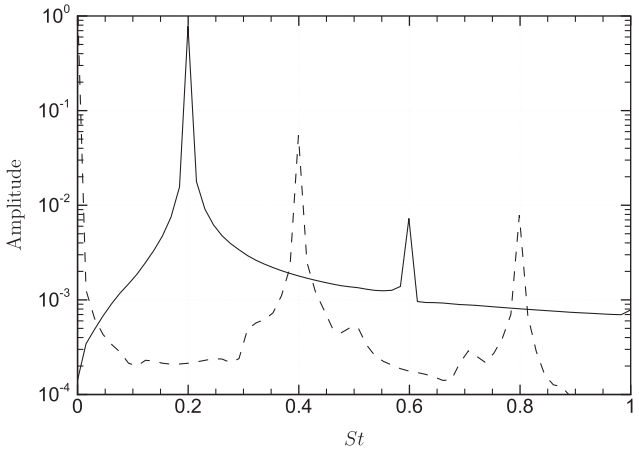

Fig. 6. Spectrum (DFT) of the lift (dashed line) and the drag (solid line) at $Re = 200$.

Table 1
Comparison of the Strouhal number and the mean drag coefficient at $Re = 200$.

Authors	S_t	C_D
Braza et al. [21]	0.2000	1.4000
Henderson [22]	0.1971	1.3412
He et al. [23]	0.1978	1.3560
Bergmann et al. [24]	0.1999	1.3900
Present study	0.1980	1.3500

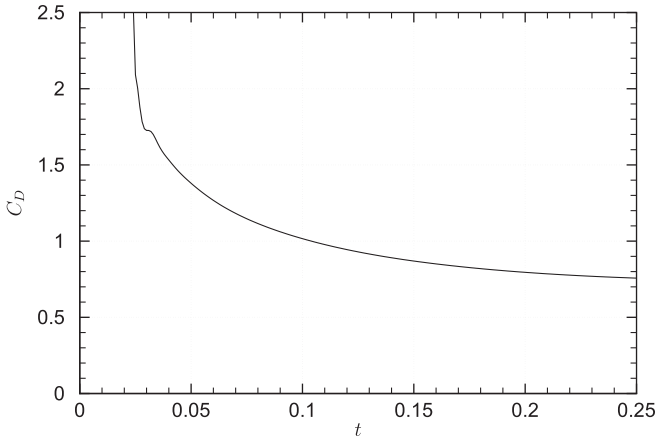

Fig. 7. Drag coefficient for an impulsively started cylinder at $Re = 550$.

In the first test case, we take $Re = 200$, $\boldsymbol{u}_s = \boldsymbol{0}$, $\boldsymbol{u}_\infty = \boldsymbol{e}_x$ and the cylinder is centered in $\boldsymbol{x} = \boldsymbol{0}$. The temporal evolution of the lift and drag coefficients is presented in Fig. 5. The amplitudes of lift and drag are approximately equal to 1.6 and 0.1, respectively, and the mean drag and the Strouhal number (Fig. 6) are in good agreements with those obtained in previous studies (see Table 1).

For the second test case, we consider an impulsively started cylinder at $Re = 550$ and we compare the force acting on the cylinder in two equivalent situations. In one configuration, the force is computed when the flow at infinity is impulsively started and the cylinder is steady, i.e., $\boldsymbol{u}_s = \boldsymbol{0}$ and $\boldsymbol{u}_\infty = \boldsymbol{e}_x$. Fig. 7 present the evolution of the drag coefficient for a short time integration, i.e., $0 \leqslant t \leqslant 0.25$. The qualitative and quantitative behavior of the curve compares favorably with the curve obtained in [25], Fig. 8. Next, we consider the invariant configuration where the cylinder is impulsively started and its speed is set to $\boldsymbol{u}_s = -\boldsymbol{e}_x$ and $\boldsymbol{u}_\infty = \boldsymbol{0}$. The cylinder is now crossing the grid as it is translating toward the left. In Fig. 8 we compare the aerodynamic coefficients obtained for the two configurations. It is seen that the overall behavior of the two curves is similar

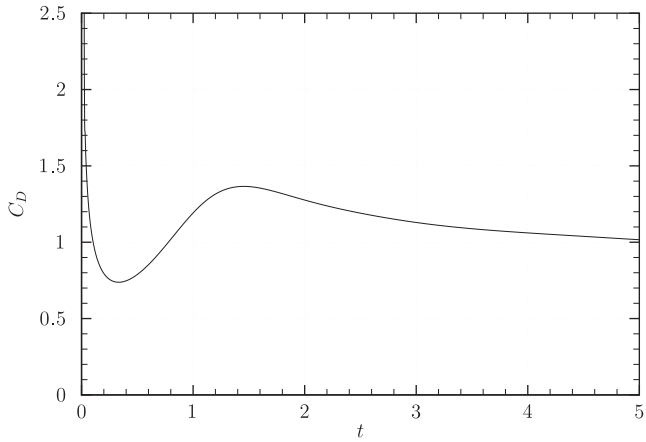

(a) $\boldsymbol{u}_\infty = \boldsymbol{e}_x$, $\boldsymbol{u}_s = \boldsymbol{0}$.

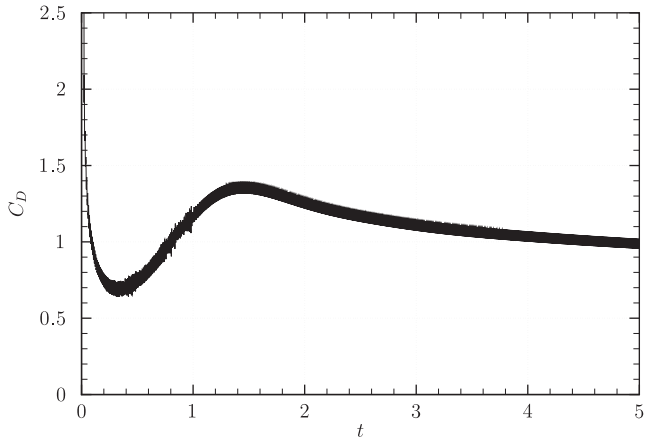

(b) $\boldsymbol{u}_\infty = \boldsymbol{0}$, $\boldsymbol{u}_s = -\boldsymbol{e}_x$

Fig. 8. Drag coefficient for an impulsively started cylinder at $Re = 550$.

and that they compare well with [25] Fig. 8, although the one relative to the translating cylinder is affected by small amplitude oscillations. This is due to the fact that in Eq. (15a) the discrete time derivative is taken over an integral whose support is varying discretely in time, and since the accuracy of the scheme is only first order, this results in oscillations of the force on the time scale of $h/\|\boldsymbol{u}_s\|$, where h is the grid size. We checked that these oscillations decrease when $h \to 0$.

4.2.3. Rigid body motion

In order to further investigate the accuracy of the results obtained for a moving body, we study the sedimentation of a two dimensional cylinder in a cavity (see Fig. 9). We consider the same geometry and flow parameters as those used in [2,14], *i.e.* the dimension of the cavity is $[0,2] \times [0,6]$, the viscosity is 0.01, the density inside and outside the cylinder is 1.5 and 1.0, the cylinder radius is 0.25 and its initial position is $(1,4)$. The time step used for the numerical simulations is $\Delta t = h/20$, where $h = \Delta y = \Delta x = 1/256$ and $h = 1/384$.

In Fig. 10 the vertical velocity profile on the horizontal line passing through the center of the cylinder at $t = 0.1$ is shown. Inside the cylinder the vertical velocity is constant at about 10.8. Fig. 11 presents the vertical cylinder velocity and the ordinate of cylinder center as a function of time. The bottom of the cavity is reached at $t \simeq 0.37$. These results are very close to those obtained in Refs. [2,14].

5. Low-order parametric modeling of fish-like swimming

5.1. Relative deformation

In this study the self-propelling objects (swimmers) have an imposed relative deformation, regardless of the force necessary to impose such relative movement. It is important to remark that since we assume that no external force is imposed,

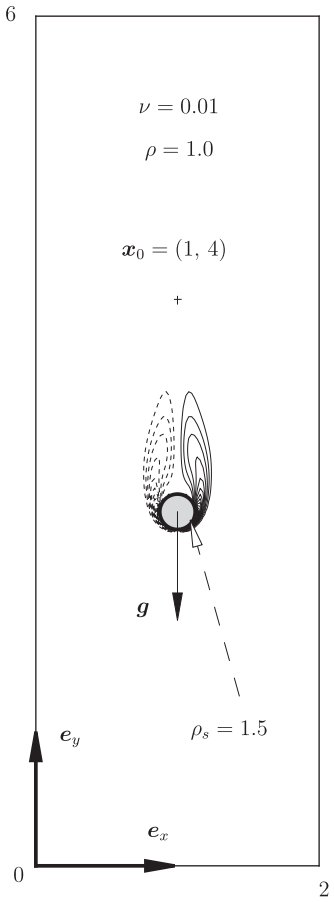

Fig. 9. Sketch of the flow configuration for the sedimentation of a the cylinder in a cavity.

the relative deformation must be such that the linear and angular momentum will only change due to flow induced forces. In other words, the class of admissible swimmer deformations $\boldsymbol{u}_i'$ must be such that

$$\int_{\Omega_i} \boldsymbol{u}_i'(\boldsymbol{x}, t)\mathrm{d}\boldsymbol{x} = 0, \tag{16}$$

$$\int_{\Omega_i} \boldsymbol{x} \wedge \boldsymbol{u}_i'(\boldsymbol{x}, t)\mathrm{d}\boldsymbol{x} = 0, \tag{17}$$

where we assume that the swimmer density is constant.

Fish-like swimming can be classified based on both body shape and locomotion modes. Three categories are described in [26]: the first is the body and caudal fin (BCF) periodic, the second is the BCF transient (turns, sudden starts, etc.), and the last one is the median and paired fin (MPF). In this study we will focus on both periodic and transient BCF modes, that can be further decomposed into four sub-categories, *i.e.* anguiliform, subcarangiform, carangiform and thunniform shapes [27,28]. After having defined the steady shape, Section 5.2, we will model the BCF periodic, Section 5.3 and then the BCF transient for turns, Section 5.4.

5.2. Modeling of the swimmer steady shape

We start with a steady symmetric shape. The swimmer shape is described by an airfoil. The most simple way to parametrize an airfoil shape is the Joukowsky transform, that transforms a circle with radius $r_c = 1$ defined by the complex number $\zeta = \eta + i\theta$ to an airfoil profile defined by the complex number $z = x_s + iy_s$ in the transformed plane. The transform is the following:

$$\xi = \zeta + \frac{1}{\zeta}. \tag{18}$$

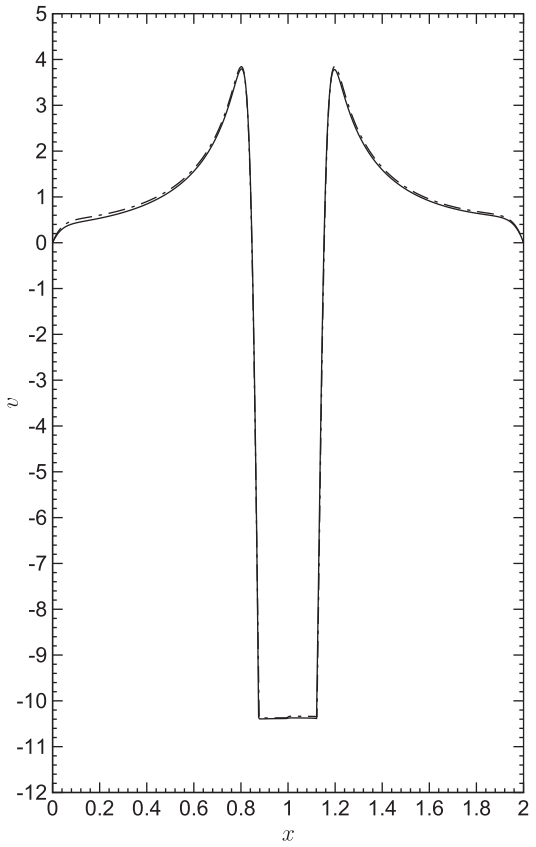

Fig. 10. Vertical velocity profile at the cylinder height at $t = 0.1$. Solid line for $h = 1/256$, dashed line for $h = 1/384$.

Since this airfoil presents a cusped trailing edge, the Karman–Trefftz transform (see Fig. 12) is further applied to retrieve more realistic shapes

$$z = n\frac{\left(1+\frac{1}{\zeta}\right)^n + \left(1-\frac{1}{\zeta}\right)^n}{\left(1+\frac{1}{\zeta}\right)^n - \left(1-\frac{1}{\zeta}\right)^n}, \tag{19}$$

where the trailing edge angle is $\alpha = (2-n)\pi$. A translation, contraction or extension of the plane z is then applied to obtain $0 \leqslant x \leqslant \ell$, ℓ being the length of the fish. At this stage the steady fish shape is defined by four parameters defining the origin of the circle (η_c and θ_c), the tail angle (α) and the body length (ℓ). Since a symmetric steady shape is desired ($\theta_c = 0$), we take $\eta_c < 0, \alpha > 0$ and $\ell \geqslant 0$ to parametrize the shape. Different fish thicknesses can be obtained varying η_c. For instance, while $\eta_c = -0.01$ approximates an anguiliform shape, $\eta_c = -0.04$ approximates a thunniform shape, and $-0.05 < \eta_c < -0.01$ approximate carangiform and subcarangiform shapes.

5.3. Modeling of BCF periodic modes

Let us now define the periodic swimming law. The idea is to deform the backbone of the steady fish (defined by $0 \leqslant x \leqslant \ell$ and $y = 0$) to fit a given curve $y(x,t)$ keeping the backbone length fixed. Let s be the curvilinear coordinate of the deformed backbone ($0 \leqslant s \leqslant \ell$). We fix $s = 0$ at $x = x_0$. For a given coordinate s, the abscissa $x(s)$ is found by inverting

$$s(x) = \int_{x_0}^{x} \sqrt{1 + \left(\frac{\partial y(x',t)}{\partial x'}\right)^2}\, \mathrm{d}x'.$$

The corresponding deformation $y(x(s),t)$ can then be computed. As described in [11], a natural imposed body periodic motion $y(x,t)$ is

$$y(x,t) = a(x)\sin(2\pi(x/\lambda + ft)), \tag{20a}$$

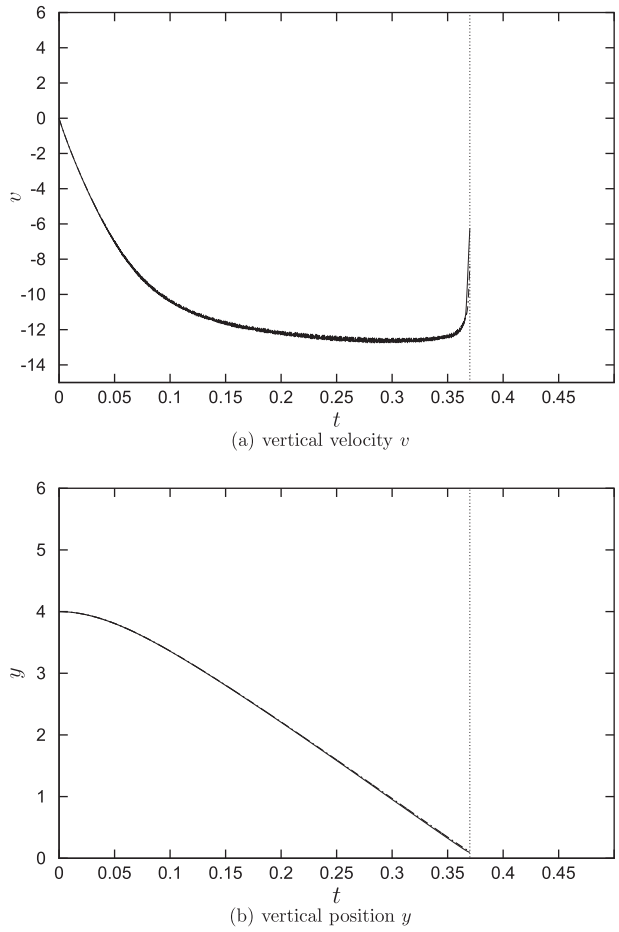

Fig. 11. Sedimentation of a two dimensional cylinder in a cavity. The simulations were stopped when the bottom of the cavity is reached at $t \simeq 0.37$. Solid lines for $h = 1/256$, dashed lines for $h = 1/384$.

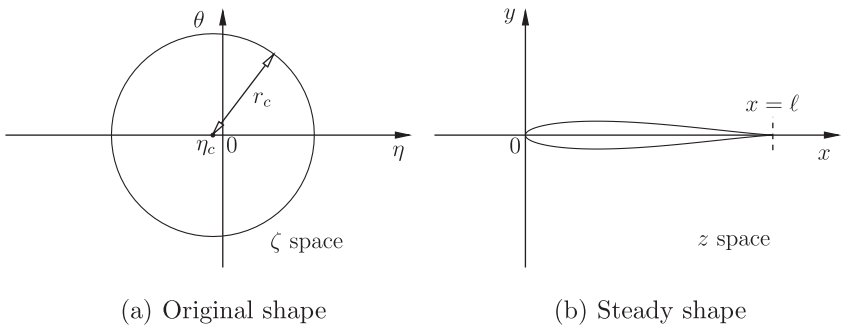

Fig. 12. Sketch of the Karman–Trefftz transform. In this example the z space is transformed to fit $0 \leqslant x_s \leqslant \ell$.

where the curve envelope is given by

$$a(x) = c_1 x + c_2 x^2. \tag{20b}$$

While the length of the fish is always equal to ℓ, the cartesian abscissa is $x(\ell) < \ell$, except for the steady configuration where $x(\ell) = \ell$. This motion is defined by a constant phase speed $c_p = \lambda f$, where λ and f denote the wavelength and the frequency of the oscillations, respectively. Note that the wavelength λ is not necessarily equal to the body length as in Ref. [29]. The wavy motion affects the swimmer from the head to the tail and can be centered on the nose of the fish [29] or at a predefined percentage δ of the body length [30]. The parameters c_1 and c_2 can thus be adjusted in order to impose a maximal tail ampli-

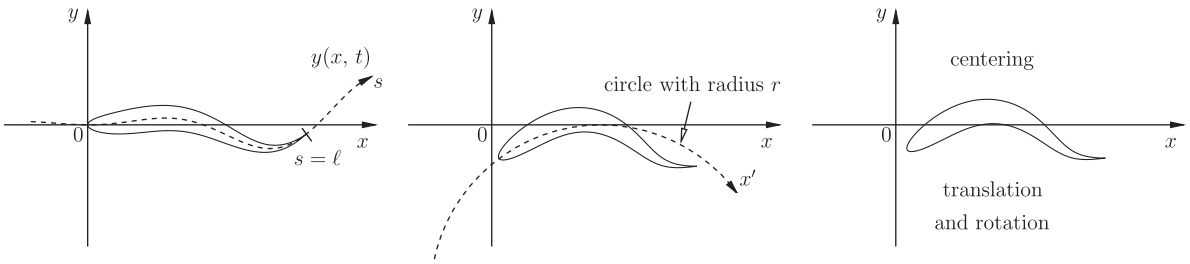

(a) Swimming shape (b) Maneuvering shape (c) Real motion shape

Fig. 13. Sketch of swimming and maneuvering shape.

tude $A/2$, which is an important parameter for the locomotion efficiency [7]. Note that in practice a transition during a short period $T = 0.2$ is performed from the initial body shape ($y(x,t) = 0$) to the full swimming law $y(x,t) = a(x)\sin(2\pi(x/\lambda + ft))$. A swimmer typical configuration is given in Fig. 13(a).

Since the shape is characterized by three parameters (denoted by $\boldsymbol{b}$) and the swim is characterized by the 5 parameters $\boldsymbol{s} = (c_1, c_2, \lambda, f, \delta)^T$, 8 parameters define the shape and swimming law. The unsteady swimming body profile is denoted $\boldsymbol{P}(\boldsymbol{b},\boldsymbol{s},t)$. Finally, the algorithm to define the swimmer deformation is

- generate a desired deformation of the swimmer centerline (fish backbone);
- perform an homothety for mass conservation;
- subtract the center of mass displacement, so that Eq. (16) is satisfied;
- subtract a rigid rotation, so that Eq. (17) is satisfied.

5.4. Modeling of BCF transient for turns

Since the swim motion defined in the previous section is periodic with zero mean deformation (we have $\int_t^{t+2\pi/f} y(x,t')\mathrm{d}t' = 0$), maneuvers are difficult. To improve the maneuverability we introduce a different strategy to modify the swimming law $y(x,t)$ to get non zero mean deformation. We chose a transform $\mathcal{R} : P(\boldsymbol{b},\boldsymbol{s},t) \mapsto P_r(\boldsymbol{b},\boldsymbol{s},t)$ such that the swimming body profile $P(\boldsymbol{b},\boldsymbol{s},t)$ rolls up onto a circle with radius r to give a new profile $P_r(\boldsymbol{b},\boldsymbol{s},t)$ (see Fig. 13(b)). We have $P_\infty(\boldsymbol{b},\boldsymbol{s},t) = P(\boldsymbol{b},\boldsymbol{s},t)$. The minimal turning radius r can vary in function of the fish considered [31]. For instance $r = 0.47\ell$ for yellowfin tuna [32], $r = 0.13\ell$ for dolphin fish *Corypaena hippurus* [33] and even $r = 0.065\ell$ for angelfish *Pterophyllum eimekei* Ahl (MPF) [34].

The final swimmer deformation shape is re-centered and rotated to avoid introducing additional forces and torques. An example of shape $P_r(\boldsymbol{b},\boldsymbol{s},t)$ is given in Fig. 13(c).

6. Numerical survey of fish-like locomotion

This section is devoted to the investigation of fish like swimming employing the numerical tools presented in the previous sections. In the following simulations we used $h = \Delta x = \Delta y = 5\Delta t$. The retained space resolution is determined on the basis of a convergence study detailed in the next section.

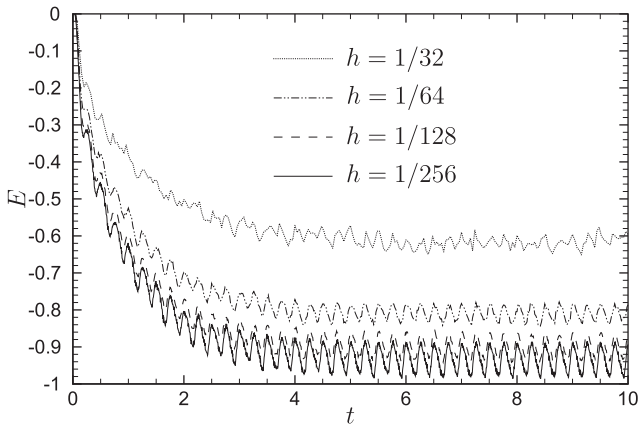

Fig. 14. Convergence of fish swimming versus the mesh size.

Table 2
Evolution of the limit average velocity $\overline{u}$, relative deviation d and computational time t_{CPU} as a function of h.

h	$\overline{u}$	d (%)	t_{CPU} (min)
1/32	−0.62	50	8
1/64	−0.81	14.8	42
1/128	−0.9	3.3	298
1/256	−0.93	0	2552

Table 3
Parameters used to model four different "fish modes".

Fish	Shape			Swimming law				
F_i	η_c	α	ℓ	c_1	c_2	λ	f	δ
F_1	−0.04	5	1	0.1	0.9	1.25	2	0
F_2	−0.03	5	1	0.4	0.6	1.00	2	0
F_3	−0.02	5	1	0.7	0.3	0.75	2	0
F_4	−0.01	5	1	1.0	0.0	0.50	2	0

6.1. Grid convergence

The motion of rigid bodies, including force and torque computation, has already been validated (Section 4.2). We are now interested in grid convergence for the motion of deformable bodies. For a convergence study the limit velocity $\overline{u}_h$ is particularly pertinent since it involves the computation of both the forces and the torques acting on the swimmer. A fish with given shape $\boldsymbol{b}$ and swimming law $\boldsymbol{s}$ is chosen (this is fish F_1 of next Section 6.2). Computations using different values of h are performed at $Re = 1000$. The fish swims over a distance equal to 9 and the evolution of the velocities u_h for $0 \leqslant t \leqslant 10$ are presented in Fig. 14. The finest mesh used corresponds to $h = 1/256$, so that in a computational domain of $[-10,2] \times [2,2]$ we have $3072 \times 1024 \simeq 3.1$ millions of mesh nodes. We take this solution as the reference solution $\overline{u}_{256}$. The relative deviation of the limit velocity $\overline{u}_h$ is then defined as $d(h) = \|\overline{u}_h - \overline{u}_{256}\|_2 / \|\overline{u}_h\|_2$. The limit velocity $\overline{u}_h$, the relative deviation $d(h)$ and the computation time t_{CPU} are reported in Table 2. The relative deviation is approximately divided by a factor of 4 when h is divided by a factor 2. Table 2 shows that $h = 1/128$ is a good compromise between the deviation (only 3.3%) and the computational time (*8* times smaller than for $h = 258$). We thus chose $h = 1/128$ for all the following simulations at $Re = 1000$.

6.2. Body and caudal fin modes (BCF)

The aim of this section is to present a study of body and caudal fin (BCF) swim modes and the influence of such modes on the energetic efficiency of the motion. We initially only consider the maximal velocity attained, without any power considerations. BCF movement can be decomposed into anguiliform, subcarangiform, carangiform and thunniform modes [27]. While the anguiliform mode presents large oscillations onto the whole thin body, the thunniform mode presents only limited oscillations of the tail of a blunt shape. Subcarangiform and carangiform modes present intermediate oscillations and shapes, between anguiliform and thunniform modes. These kind of BCF modes are modeled using the parametric representation of Section 5. The overall swimmer displacement is strongly influenced by the initial tail stroke, i.e., the mean lateral velocity is non zero if special care is not taken for the initial tail transient. In order to obtain a zero mean lateral velocity we use the transient introduced in Section 5.4 where the radius r is proportional to the vertical deviation of the center of mass Δy_G, *i.e.* $r \propto \Delta y_G$, being $y_G(t = 0) = 0$.

Each swim mode is modeled using a different body shape and swimming law. As described in Section 5, the modes are defined by 8 parameters in this study. We chose four sets of parameters that correspond to swimming modes and shapes called F_1, F_2, F_3 and F_4, representing thunniform, carangiform, subcarangiform and anguiliform modes, respectively. All the parameters defining both shapes and swimming laws are reported in Table 3. Note that we chose to use the same tail angle $\alpha = 5$, length $\ell = 1$, frequency $f = 2$ and $\delta = 0$. Only the shape thickness (defined by η), the swimming law envelop (defined by c_1 and c_2) as well as the wavelength λ are modified. Note that c_1 and c_2 are rescaled to obtain a tail displacement amplitude $A = 0.4$. All the simulation are performed independently, and each simulation is stopped when the fish has travelled a distance equal 9 times the body length. The associated time is noted T_9. An isovorticity representation of each wake is given in Figs. 15 and 16 for $Re = 10^3$ and $Re = 10^4$, respectively. Inverted Karman streets can be observed (more pronounced at $Re = 10^3$ than at $Re = 10^4$).

Table 4 summarizes the results in terms of time T_9 to reach the distance $d = 9$, exit velocity U_{max}, maximum acceleration γ_{max} and average velocity $\overline{U}$ at $Re = 10^3$ and $Re = 10^4$. The maximum acceleration is however dependent on the (linear) transient we imposed from $t = 0$ to $t = 0.2$.

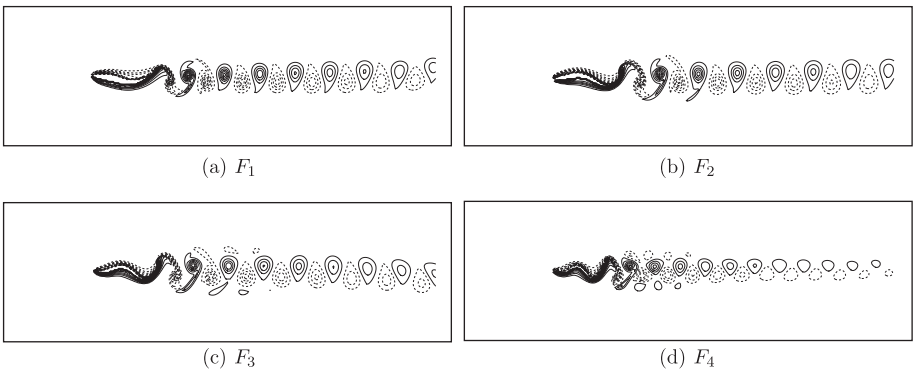

(a) F_1 (b) F_2 (c) F_3 (d) F_4

Fig. 15. Vorticity representation of the wakes generated by some BCF like swimming movements at $Re = 10^3$. All the figures are plotted for $-100 \leqslant \omega_z \leqslant 100$.

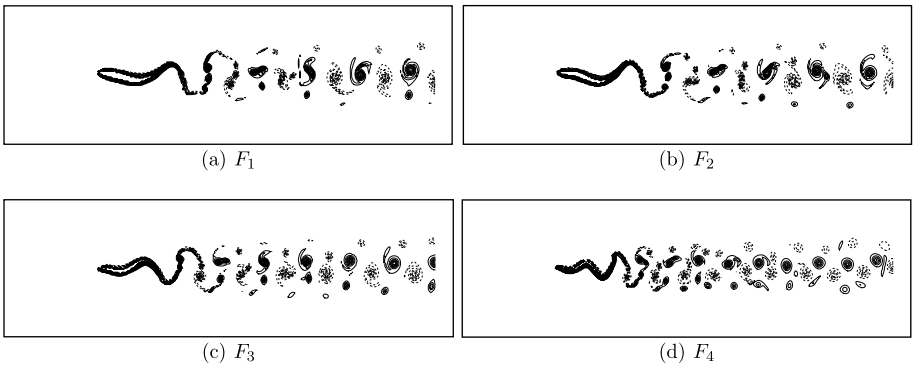

(a) F_1 (b) F_2 (c) F_3 (d) F_4

Fig. 16. Vorticity representation of the wakes generated by some BCF like swimming movements at $Re = 10^4$. All the figures are plotted for $-100 \leqslant \omega_z \leqslant 100$.

6.3. On the power required to swim

An important issue is to classify the four swimmers introduced in the above section in terms of efficiency. We denote σ' the dimensionless viscous stress tensor, so that $\sigma'_{ij} = \frac{1}{Re}(\frac{\partial u_j}{\partial x_i} + \frac{\partial u_i}{\partial x_j})$. In dimensionless form, the power required for the swim is:

$$P(t) = -\int_{\partial\Omega_i} p\boldsymbol{u}\cdot\boldsymbol{n}\mathrm{d}S + \int_{\partial\Omega_i}(\sigma'\cdot\boldsymbol{n})\cdot\boldsymbol{u}\mathrm{d}S. \tag{21}$$

Since the mesh is not body fitted, $P(t)$ cannot be computed using Eq. (21). By integrating on the fluid domain Ω_f the scalar product of the momentum equations and the velocity vector, the power can be written as:

$$P(t) = \frac{\partial}{\partial t}\int_{\Omega_f}\frac{u^2}{2}\mathrm{d}\Omega + \frac{1}{Re}\int_{\Omega_f}\sigma'_{ij}\frac{\partial u_i}{\partial x_j}\mathrm{d}\Omega. \tag{22}$$

The power required to swim is equal then to the temporal variation of the kinetic energy in the flow domain plus the power dissipated by viscosity. We denote T_k the time required to reach a distance equal to $d = 9$ unit lengths. The energy required for fish F_k to travel the distance d is $E^{(k)} = \int_{T_k} P^{(k)}\mathrm{d}t$. However, the amount of energy spent per unit time is of course a function of velocity. If all the swimmer have the same velocity U_r of the slowest (F_4), we can classify the swimmers for maximum endurance. The maximum tail amplitude A is hence modified such that at each iteration, if $U > U_r$ we decrease A proportionally, and vice versa. We call F_1^r, F_2^r and F_3^r the swimmers corresponding to F_1, F_2 and F_3 with velocity regulator. Table 5 presents the energy required to displace the swimmers of a given distance. The most efficient swimmer is F_1^r for both Reynolds numbers.

In the well known study of Gray in 1936 [35] it was observed that some aquatic vertebrates (dolphins) are able to swim at surprisingly high speeds. In order to investigate the swimming efficiency, the approximate power required to tow the dolphin at such speed was compared to an estimate of the available muscular power. Gray argued that the power required for a dolphin of length 1.82 m to swim at a speed of 10.1 m/s is about seven times the muscular power available for propulsion. Some of the assumptions made to get to these conclusions appear now to be flawed [36]. It is interesting, therefore, to

Table 4
Maximal velocity $|U_{max}|$, maximal acceleration $|\gamma_{max}|$ and average velocity $|\overline{U}|$ at $Re = 10^3$ and $Re = 10^4$.

Fish	$Re = 10^3$				$Re = 10^4$			
	$\lvert U_{max}\rvert$	$\lvert\overline{U}\rvert$	$\lvert\gamma_{max}\rvert$	T_9	$\lvert U_{max}\rvert$	$\lvert\overline{U}\rvert$	$\lvert\gamma_{max}\rvert$	T_9
F_1	0.91	0.83	3.3	10.81	1.42	1.22	3.4	7.37
F_2	0.97	0.93	4.6	9.70	1.39	1.27	4.9	7.06
F_3	0.92	0.89	7.5	10.13	1.18	1.14	8.0	7.88
F_4	0.65	0.63	9.5	14.2	0.81	0.79	10.4	11.4

Table 5
Comparison of the energy $E^{(k)}$ required to travel the distance $d = 9$ at $Re = 10^3$ and $Re = 10^4$. Fishes F_1^r, F_2^r, F_3^r regulated the maximal tail amplitude to swim at the velocity of F_4.

Fish	$Re = 10^3$	$Re = 10^4$
F_1^r	0.64	0.24
F_2^r	0.66	0.26
F_3^r	0.77	0.28
F_4^r	0.77	0.30

Table 6
Propulsive indexes I_p evaluated for fishes F_1,F_2,F_3 and F_4 at $Re = 10^3$ and $Re = 10^4$.

Fish	$Re = 10^3$	$Re = 10^4$
F_1	0.26	0.31
F_2	0.26	0.21
F_3	0.24	0.17
F_4	0.17	0.14

compare the power necessary to tow a swimmer to the one actually developed by the deformable body to swim at the same speed.

We denote P_{sps} the mean power required for a given a steady periodic swimming at a velocity U, and P_{tow} the mean power need to tow the same rigid body at the same velocity U. Powers P_{sps} and P_{tow} are computed from (22). Following [11], we defined the propulsive index I_p as being the ratio P_{tow} and P_{sps},

$$I_p = \frac{P_{tow}}{P_{sps}}. \tag{23}$$

Drag reduction is achieved if $I_p > 1$. The propulsive indexes evaluated for swimmers F_1, F_2, F_3 and F_4 at $Re = 10^3$ and $Re = 10^4$ are reported in Table 6. In our laminar two-dimensional configuration we do not obtain any drag reduction (I_p is always below unity). The power required to swim is three to eight times higher than that required to tow the rigid bodies. The results that we obtain are of course not conclusive since we develop our simulations in a two-dimensional setting in a laminar flow regime. Also, we do not model fins or other appendages that are crucial in actual fish swimming.

It is also of interest to investigate if burst-and-coast swimming can lead to energetic advantages [37,38]. The process we employed is similar to that described in Ref. [37]. We assume that at $t = t_0$ the rigid fish body has a velocity equal to U_i. A swimming period starts from $t = t_0$ until $t_1 = t_0 + T_b$ that correspond to the time when fish reached a given maximal velocity U_f. Then a new period starts and the propulsive motion of the fish stops. The fish glides as a rigid body and the velocity decreases from U_f at t_1 to its minimal velocity U_i at $t_2 = t_1 + T_c$. A new burst-and-coast period $T = T_b + T_c$ starts again. The swimming efficiency depends *a priori* on the choice of U_f and U_i [37,38].

In what follows we will study swimmer F_1 at $Re = 10^3$ and $Re = 10^4$. At each Reynolds number four test cases are considered. We denote $U_f = \alpha_f U_{max}$ and $U_i = \alpha_i U_{max}$, where U_{max} is the maximal velocity reached by F_1 using steady periodic swimming with $A/2 = 0.2$ (see Table 4). We initially consider a relevant difference between U_f and U_i, *i.e.* we chose $\alpha_f = 0.8$ and $\alpha_i = 0.2$. Then, we investigate smaller differences for high velocities ($\alpha_f = 0.8$ and $\alpha_i = 0.6$), medium velocities ($\alpha_f = 0.6$ and $\alpha_i = 0.4$) and small velocities ($\alpha_f = 0.4$ and $\alpha_i = 0.2$). For burst and coast swimming, the amplitude grows linearly until the limit $A/2 = 0.2$ in the burst period, and then the amplitude decrease linearly to zero for coast period. Following previous studies [39], we denote R ratio between burst and coast swimming mean power P_{bac} (with average velocity $\overline{U}$) and steady swimming mean power P_{sps} (at same velocity $\overline{U}$ using regulation of the tail amplitude):

$$R = \frac{P_{bac}}{P_{sps}}. \tag{24}$$

Table 7
Efficiency R of burst and coast swimming for fish F_1 at $Re = 10^3$ and $Re = 10^4$ using different couples of $U_f = \alpha_f U_{max}$ and $U_i = \alpha_i U_{max}$.

(α_i, α_f)	$Re = 10^3$	$Re = 10^4$
(0.2, 0.8)	0.77	0.85
(0.6, 0.8)	1.02	1.00
(0.4, 0.6)	0.85	0.81
(0.2, 0.4)	0.63	0.71

Note that in both cases we also impose deformation such that the swimmer follows a straight trajectory (the center of mass is approximately kept at a fixed coordinate y). Both parameters used and results are shown in Table 7. For almost all cases considered, the burst and coast swimming is more efficient than steady periodic swimming. The efficiency of burst and coast swimming increases when the average swimming velocity decreases. The results are in good agreements with [39].

6.4. Turns and maneuvers

In this section we explore the maneuverability of swimmers. It is of interest to study how swimmers can turn abruptly in some direction. The objective is not for the moment to understand complex real fishes motion but only to study a prototype motion for robots. We show the effectiveness of a simple control based on both the deformation introduced in Section 5.4 and the angle of vision θ_f. This angle is arbitrarily defined as being the oriented angle between the line passing through the center of mass of the fish and leading edge and the line passing through the leading edge and the objective (food), see Fig. 17.

If $\theta_f = 0$ (objective straight forward), we want to recover $P_r(\boldsymbol{b},\boldsymbol{s},t) \to P(\boldsymbol{b},\boldsymbol{s},t)$, *i.e.* $r \to \infty$. Note that in practice we do not impose $r \to \infty$, but we shift from profile $P_r(\boldsymbol{b},\boldsymbol{s},t)$ to profile $P(\boldsymbol{b},\boldsymbol{s},t)$. For physical reasons we have to impose $|r| \geqslant \overline{r}$. We choose $\overline{r} = 0.5$ that is approximately the turning radius for tuna [32]. We suppose that this limit can be reached for any $|\theta_f| \geqslant \overline{\theta_f}$. In this study we choose $\overline{\theta} = \pi/4$. We have also to impose a a relation $r(\theta_f)$ for $|\theta_f| \leqslant \overline{\theta_f}$. We choose $r(\theta_f) = \overline{r}(\frac{\overline{\theta}}{\theta_f})^2, \forall 0 < |\theta_f| < \overline{\theta_f}$

$$r(\theta_f) = \begin{cases} \infty & \text{if } \theta_f = 0, \\ \overline{r} & \text{if } \theta_f \geqslant \overline{\theta_f}, \\ -\overline{r} & \text{if } \theta_f \leqslant -\overline{\theta_f}, \\ \overline{r}\left(\frac{\overline{\theta}}{\theta_f}\right)^2 & \text{otherwise.} \end{cases} \tag{25}$$

The results are illustrated in Fig. 18 for swimmer F_1 at $Re = 10^3$. The initial positions of the leading and trailing edge are $(0,0)$ and $(\ell,0)$, respectively, and the food is located at $(2,-1)$. The initial angle of vision is then $\theta_f = 2\pi - \arctan 1/2 \approx 0.85\pi$ so that $r(t=0) = \overline{r}$. Note that a transition during a short time $T = 0.2$ is performed for the deformation from $r \to \infty$ (initial position) to $r = f(\theta_f)$.

6.5. Influence of group swimming on the locomotion efficiency

It was demonstrated that fishes can exploit the vortices present in the flow to reduce the energy required for the locomotion (see for instance [40]). More surprisingly, even dead fish can exploit vortex wakes [12] to swim. The aim of this section is thus to study the interactions between several swimmer wakes and to understand how a fish school can organize itself to improve performance or to decrease the power spent for the locomotion [41]. In what follows, all swimmers are supposed to have the same swimming law and shape. Let D be the lateral distance between two swimmers. This distance tends to decrease due to Venturi-like effect. We therefore use the deformation introduced in the previous section in order to keep approximately constant the horizontal distance between the swimmers by taking a curvature of the swimmer that is proportional to the horizontal distance between the swimmers.

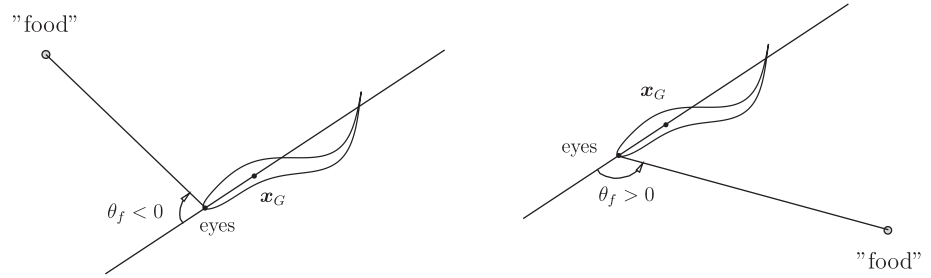

Fig. 17. Sketch of the oriented food angle of vision.

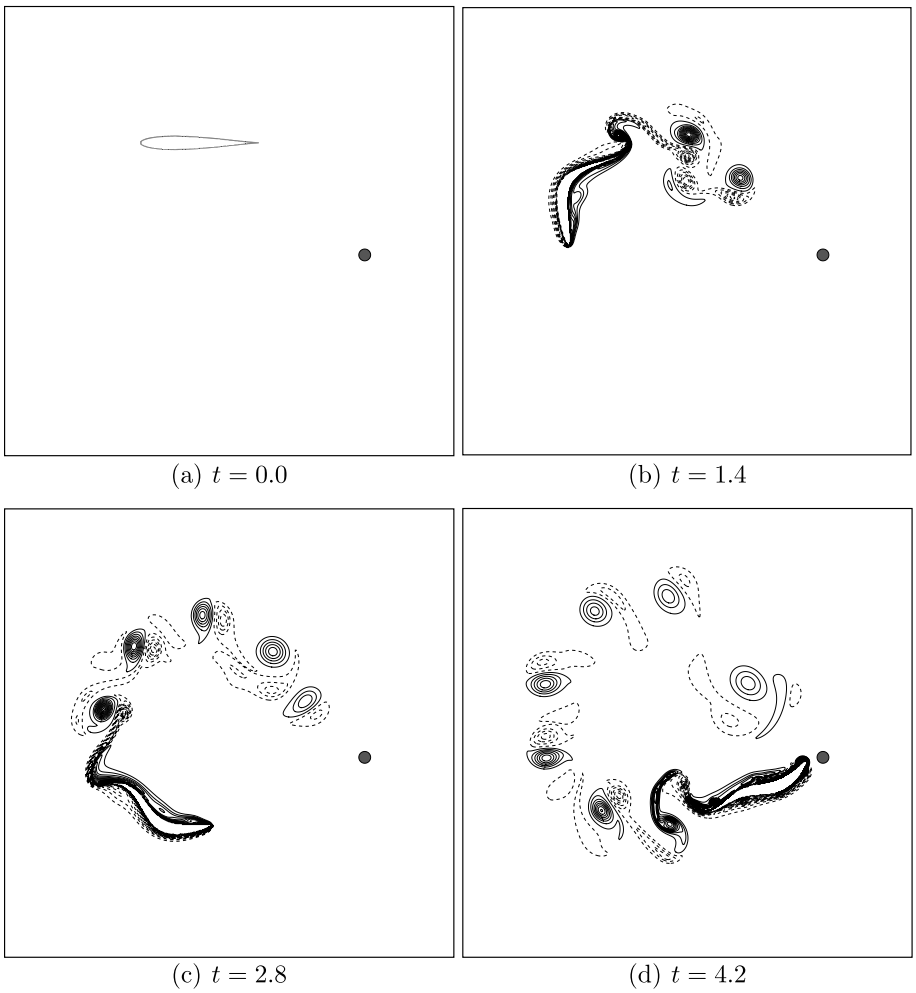

Fig. 18. Snapshots of the fish maneuvers to reach the gray circle "food" at $Re = 10^3$. All the figures are plotted for $-100 \leqslant \omega_z \leqslant 100$.

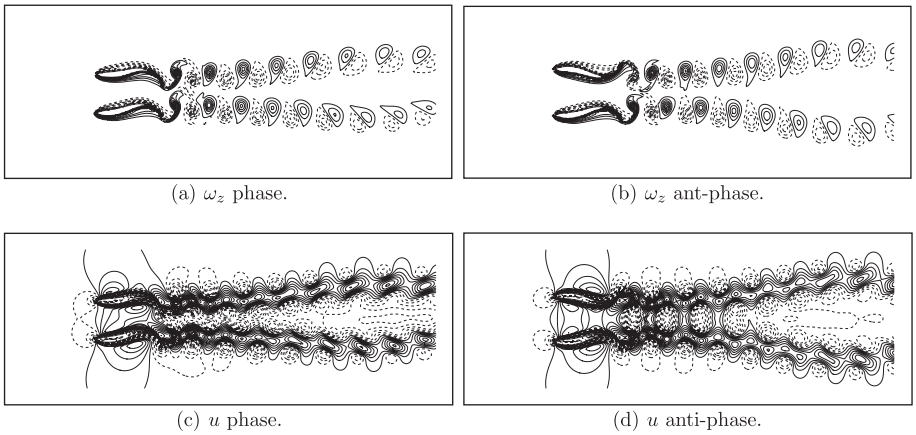

Fig. 19. Wakes generated by to frontal fishes F_1 at $Re = 10^3$ with $D = 0.5$. Left and right pictures correspond to phase and anti-phase fishes, respectively. $-100 \leqslant \omega_z \leqslant 100$, $-1.1 \leqslant u \leqslant 0.7$.

We first study the wake generated by a pair of swimmers initially located at points $(0, -D/2)$ and $(0, D/2)$, respectively. Both in-phase and anti-phase swimming laws are considered and Fig. 19(a) and (b) shows an isovorticity representation

Table 8
Percentage of energy saved for the three-swimmer school in comparison with three independent swimmers. $Re = 10^3$.

LD	Phase				Anti-phase			
	0.4	0.5	0.6	0.7	0.4	0.5	0.6	0.7
1.5	15.0	16.3	11.1	7.1	6.8	6.9	9.8	7.1
2.0	10.1	14.5	9.8	6.0	6.8	6.1	9.8	6.0
2.5	8.4	13.6	9.0	5.1	6.7	5.3	9.0	5.1
3.0	15.0	15.1	6.9	5.0	5.2	5.1	7.0	3.2
3.5	5.2	13.2	6.2	2.2	4.9	5.0	6.2	0.5

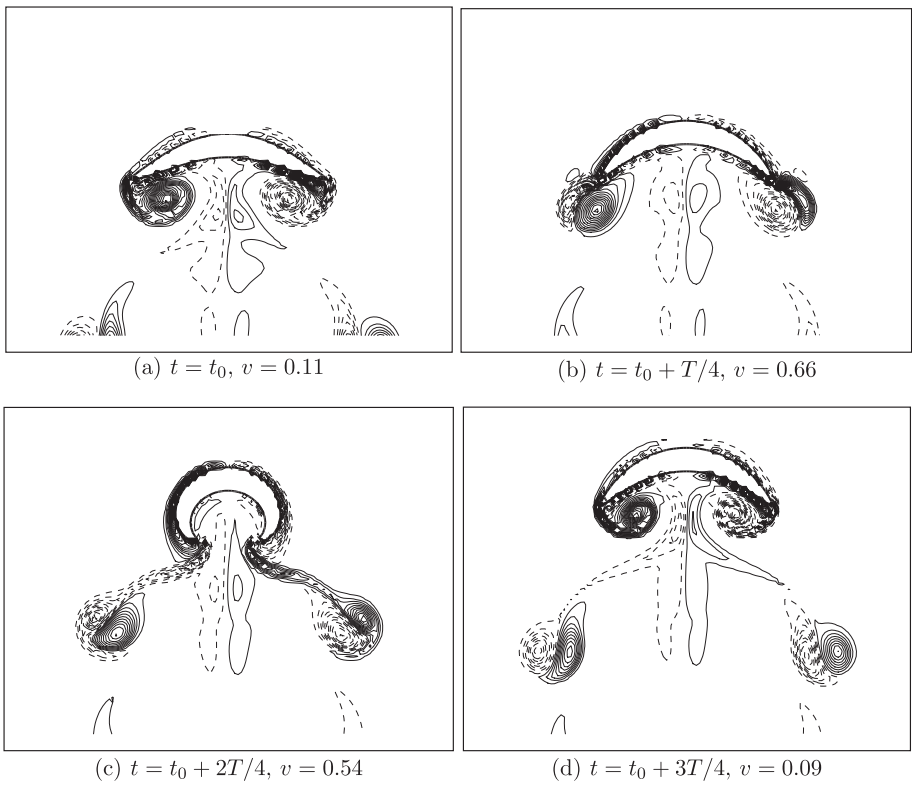

Fig. 20. Vorticity representation of the wake generated by a jellyfish like swimming at $Re = 10^3$. All the figures are plotted for $-100 \leqslant \omega_z \leqslant 100$.

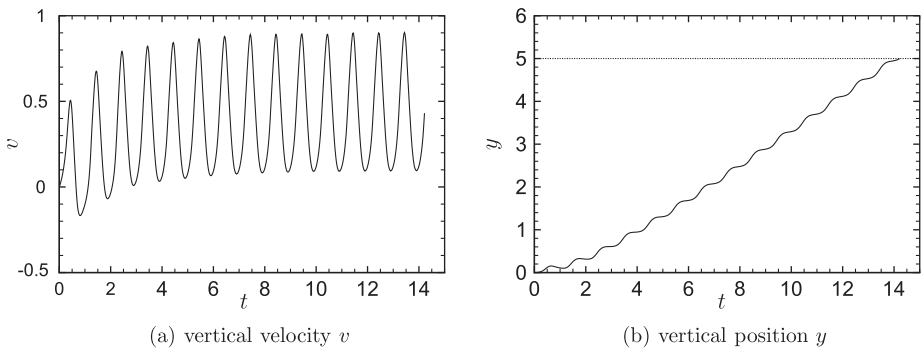

Fig. 21. Temporal evolution of the vertical velocity and position for the jellyfish at $Re = 10^3$.

of the wake generated by two swimmers separated by a distance $D = 0.5$. The isovalues of horizontal velocity are plotted in Fig. 19(c) and (d). In both cases a zone of negative velocity exists in the wake of the two swimmers. In what follows we denote L the longitudinal distance between a third swimmer and the leading swimmers pair. The amplitude of the caudal

movement of the swimmer in the wake is regulated so that it cannot overcome the first two. Hence L and D are approximately constant all along the swim. Table 8 summarizes the energy savings that can be obtained by a three-swimmer schooling for different value of $0.3 \leqslant D \leqslant 0.7$ and $2 \leqslant L \leqslant 3.5$ at $Re = 10^3$. The most efficient configuration is obtained with in-phase swimming. For the anti-phase configuration the results weakly depend on D and L. In fact, the third swimmer has to be in phase with the wake generated by the first two swimmers and not necessarily in phase with the two swimmer deformation. Of course in the limit $D \to \infty$ and/or $L \to \infty$ there is no interaction between the swimmers and so no energy can be saved.

6.6. Another example: jellyfish-like swimming

The jellyfish like swimming is the final example of bio-locomotion we present. The jellyfish shape is modeled using a modified Karman–Trefftz transform. We start with an ellipse center at (0,0) in the complex plan (η_c, θ_c) to get a symmetric lentil like profile, rescaled to fit a length ℓ. We slightly deform this profile at the "tails" using frequency $f = 1$. We then roll up this new profiles onto circles with radius $r_c(t)$. In this study $r_c(t)$ oscillates periodically between circles with radius $r_c^{min} = 0.75$ and $r_c^{max} = 1.5$ with frequency $f = 1$.

The vortex street generated by this jellyfish like swimming is similar to that observed experimentally in Ref. [42], especially the pairing of two opposite sign vortices (see Fig. 20). Our results are also in qualitative good agreements with numerical results recently obtained for hydromedusa *Aequorea victoria* (see [43]). The temporal evolutions of vertical velocity and position are presented in Fig. 21. The simulation is stopped when the jellyfish reached $y = 5$ (the initial position was $y = 0$). The mean velocity is 0.5 and the propulsive index is $I_p = 0.58$. This quite high value (in comparison with fishes values, see Table 6) comes from the fact that the power required to tow vertically the mean jellyfish profile ($r_c = (r_c^{min} + r_c^{max})/2$) reaches also a quite high value.

7. Conclusions

In this paper we employed a simple and fast method to solve the two-dimensional laminar flow around moving and deformable bodies. Instead of body fitted meshes, we used cartesian meshes and penalization to take into account boundary conditions at solid walls. The fluid–solid interfaces are tracked using level-set functions and the motion of the bodies are computed from Newton's laws. The main advantage of this approach is its simplicity in dealing with moving bodies, the possibility of exploiting fast numerical solvers and a straight forward parallelization. The disadvantages are mainly linked to the possibility of resolving thin boundary layers and the implementation of turbulence modeling. Octree mesh adaptation or multigrid are possible improvements in these directions.

In order to illustrate the effectiveness of the numerical modeling proposed, we investigated the two-dimensional laminar flows pertinent to fish-like swimming. The swimmers are modeled using Karman–Trefftz airfoil profiles and periodic deformation laws are imposed to mimic self-propulsion. It was shown that swim modes affect energetic efficiency and that the swimmers can exploit upstream wakes to decrease the effort and to indefinitely track a prey [40]. As an additional demonstration of the versatility of the method, a jellyfish like swimming is modeled. The results obtained are in qualitative accordance with experimental visualizations [42].

The conclusions about efficiency of swimming laws that we investigated or about maneuvering cannot be extrapolated to three-dimensional fish-like swimming. Among the reasons for that is the characteristic nature of the vortex pattern in two dimensions. In three-dimensional flows instabilities in the transverse direction rapidly lead to annular vortex structures (see for example [15,16]) that disrupt the ordered succession of vortices observed in two-dimensional flows. Indeed, preliminary three-dimensional results obtained by the present approach show that the maneuvering strategies devised in two-dimensional configurations are much less effective in three dimensions.

The present study represents a step in the direction of simulating complex three-dimensional flows past moving elastic or visco-elastic bodies. A variety of flow patterns can result from the passive interaction of elastic appendages and the fluid. It will be possible in particular to model flexible fish fins and their interaction with the flow during sharp movements, with the objective for example of unveiling the mechanisms at the base of fish-locomotion efficiency.

Acknowledgment

This work has been supported by French National Research Agency (ANR) through COSINUS program (project CARPEINTER n°ANR-08-COSI-002).

References

[1] R. Mittal, G. Iaccarino, Immersed boundary methods, Annu. Rev. Fluid Mech. 37 (2005) 239–261.
[2] R. Glowinski, T.-W. Pan, T. Hesla, D. Joseph, J. Périaux, A fictitious domain approach for the direct simulation of incompressible fluid flow past moving rigid bodies: application to particulate flow, J. Comput. Phys. 169 (2001) 363–426.
[3] J. Janela, A. Lefebvre, B. Maury, A penalty method for the simulation of fluid–rigid body interaction, ESAIM Proc. 14 (2005) 201–212.
[4] P. Angot, C. Bruneau, P. Fabrie, A penalization method to take into account obstacles in a incompressible flow, Numer. Math. 81 (4) (1999) 497–520.
[5] M. Lighthill, Note on the swimming of slender fish, J. Fluid Mech. 9 (1960) 305–317.
[6] M. Lighthill, Hydromechanics of aquatic propulsion: a survey, Annu. Rev. Fluid Mech. 1 (1969) 413–446.

[7] M. Lighthill, Aquatic animal propulsion of high hydrodynamical efficiency, J. Fluid Mech. 44 (1970) 265–301.
[8] M. Lighthill, Large amplitude elongated-body theory of fish locomotion, Proc. R. Soc. Mech. B 179 (1971) 125–138.
[9] J. Sparenberg, Survey of the mathematical theory of fish locomotion, J. Eng. Math. 44 (2002) 395–448.
[10] S. Alben, Simulating the dynamics of flexible bodies and vortex sheets, J. Comput. Phys. 228 (7) (2009) 2587–2603.
[11] D. Barrett, M. Triantafyllou, D. Yue, M. Grosenbauch, M. Wolfgang, Drag reduction in fish-like locomotion, J. Fluid Mech. 392 (1999) 182–212.
[12] D. Beal, F. Hover, M. Triantafyllou, J. L.G.V. Liao, Passive propulsion in vortex wakes, J. Fluid Mech. 549 (2006) 385–402.
[13] C. Peskin, Flow patterns around heart valves: a numerical method, J. Comput. Phys. 10 (1972) 252–275.
[14] M. Coquerelle, G. Cottet, A vortex level set method for the two way coupling of an incompressible fluid with colliding rigid bodies, J. Comput. Phys. 227 (21) (2008) 9121–9137.
[15] A.A. Shirgaonkar, M.A. MacIver, N.A. Patankar, A new mathematical formulation and fast algorithm for fully resolved simulation of self-propulsion, J. Comput. Phys. 228 (7) (2009) 2366–2390.
[16] O.M. Curet, I.K. AlAli, M.A. MacIver, N.A. Patankar, A versatile implicit iterative approach for fully resolved simulation of self-propulsion, Comput. Methods Appl. Mech. Eng. 199 (2010) 2417–2424.
[17] J. Sethian, Level Set Methods and Fast Marching Methods: Evolving Interfaces in Computational Geometry, Fluid Mechanics, Computer Vision and Material Science, Cambridge University Press, 1999.
[18] A. Chorin, Numerical solution of the Navier–Stokes equations, Math. Comput. 22 (1968) 745–762.
[19] R. Temam, Sur l'approximation de la solution des equations de Navier–Stokes par la méthode des pas fractionnaires ii, Arch. Ration. Mech. Anal. 32 (1969) 377–385.
[20] F. Chantalat, C.-H. Bruneau, C. Galusinski, A. Iollo, Level-set, penalization and cartesian meshes: a paradigm for inverse problems and optimal design, J. Comput. Phys. 228 (17) (2009) 6291–6315.
[21] M. Braza, P. Chassaing, H. Ha Minh, Numerical study and physical analysis of the pressure and velocity fields in the near wake of a circular cylinder, J. Fluid Mech. 165 (1986) 79.
[22] R. Henderson, Nonlinear dynamics and pattern formation in turbulent wake transition, J. Fluid Mech. 352 (1997) 65–112.
[23] J.-W. He, R. Glowinski, R. Metcalfe, A. Nordlander, J. Périaux, Active control and drag optimization for flow past a circular cylinder. Part 1. Oscillatory cylinder rotation, J. Comput. Phys. 163 (2000) 83–117.
[24] M. Bergmann, L. Cordier, J.-P. Brancher, Optimal rotary control of the cylinder wake using proper orthogonal decomposition reduced-order model, Phys. Fluids 17 (2005) 097101.
[25] P. Ploumhans, G. Winckelmans, Vortex methods for high-resolution simulations of viscous flow past bluff bodies of general geometry, J. Comput. Phys. 165 (2) (2000) 354–406.
[26] P. Webb, Body form, locomotion and foraging in aquatic vertebrates, Am. Zool. 24 (1984) 107–120.
[27] C. Lindsey, in: W.S. Hoar, D.J. Randall (Eds.), Form, Function and Locomotory Habits in Fish, Academic, New York, 1978.
[28] M. Sfatiotakis, D.B.D.J. Lane, Review of fish swimming modes for aquatic locomotion, IEEE J. Ocean. Eng. 24 (2) (1999) 237–252.
[29] J. Deng, X.M. Shao, Z.S. Yu, Hydrodynamic studies on two traveling wavy foils in tandem arrangement, Phys. Fluids 19 (2007) 113104.
[30] Q. Zhu, M. Wolfgang, D. Yue, M. Triantafyllou, Three-dimensional flow structures and vorticity control in fish-like swimming, J. Fluid Mech. 468 (2002) 1–28.
[31] R. Blake, Fish functional design and swimming performance, J. Fish Biol. 65 (2004) 1193–1222.
[32] R. Blake, L. Chatters, P. Domenici, Turning radius of yellowfin thuna (*Thunnus albacares*) in unsteady swimming maneuvers, J. Fish Biol. 46 (1995) 536–538.
[33] P. Webb, R. Keyes, Division of labour between median fins in swimming dolphins (pisces: Coryphaeidae), Copiea (1981) 901–904.
[34] P. Domenici, R. Blake, The kinematics and performance of the scape response in the angelfish (*Pterophyllum eimekei*), Can. J. Zool. 156 (1991) 187–205.
[35] J. Gray, Studies in animal locomotion. VI. The propulsive power of the dolphin, J. Exp. Biol. 13 (1936) 192–199.
[36] F. Fish, G. Lauder, Passive and active flow control by swimming fishes and mammals, Annu. Rev. Fluid Mech. 38 (2006) 193–224.
[37] D. Weihs, Energetic advantages of burst swimming of fish, J. Theor. Biol. 48 (1974) 215–229.
[38] J. Videler, D. Weihs, Energetic advantages of burst-and-coast swimming of fish at high speeds, J. Exp. Biol. 97 (1982) 169–178.
[39] S. Stöcker, D. Weihs, Optimization of energetic advantages of burst swimming of fish, Math. Methods Appl. Sci. 24 (2001) 1387–1400.
[40] J. Liao, D. Beal, G. Lauder, M. Triantafyllou, Fish exploiting vortices decrease muscle activity, Science 302 (2003) 1566–1569.
[41] D. Weihs, P. Webb, in: P.W. Webb, D. Weihs (Eds.), Optimization of Locomotion, Praeger, New York, 1983.
[42] J. Dabiri, S. Colin, J. Costello, M. Gharib, Flow patterns generated by oblate medusan jellyfish: field measurements and laboratory analyses, J. Exp. Biol. 208 (2005) 1257–1265.
[43] M. Sahin, K. Mohseni, An arbitrary Lagrangian–Eulerian formulation for the numerical simulation of flow patterns generated by the hydromedusa *Aequorea victoria*, J. Comput. Phys. 228 (12) (2009) 4588–4605.